Supporting Information

Theoretical insights into layered IrO_2 for the oxygen evolution reaction

Xian Zhong,[a] Xin-He Liu,[a] Hong-Jie Peng*[a] and Xinyan Liu*[a,b]

[a.] Institute of Fundamental and Frontier Sciences, University of Electronic Science and Technology of China, Chengdu 611731, China.

[b.] Key Laboratory of Quantum Physics and Photonic Quantum Information, Ministry of Education, University of Electronic Science and Technology of China, Chengdu 611731, China.

* Corresponding author. E-mail: hjpeng@uestc.edu.cn; xinyanl@uestc.edu.cn

1. Methods and Computational Details

1.1. Structural optimizations

The structural optimizations were performed with DFT, with a periodic plane-wave implementation using Vienna ab initio Simulation Package (VASP) code.[1, 2] The exchange correlation energy was modelled by using Perdew–Burke–Ernzerhof (PBE) functional[3] within the generalized gradient approximation (GGA). The projector augmented wave (PAW) pseudo-potentials were used to describe ionic cores.[4] An energy cutoff of 500 eV was adopted, with a Methfessel-Paxton order one smearing of 0.05 eV applied to the orbital occupation during the geometry optimization and for the energy computations. Spin-polarization was enabled for all calculations.

The adsorption energies on the (110) facet of rutile-IrO_2 were evaluated using four-layer 2×2 supercells, while the ones on the layered IrO_2 were modeled with three-layer 2×2 (1T, 1Tr, 2H, 2Hr, 3R) and 2×3 (3Rr) supercells. The bottom one layer was constrained for the defected 3R-IrO_2 while the bottom two layers were constrained for all other structures. The [6×6×1] Monkhorst-Pack *k*-point grids were used[5] with a convergence threshold of 10^{-5} eV for the iteration in self-consistent field (SCF). All structures were optimized until force components were less than 0.02 eV $Å^{-1}$.

1.2. Electronic structure calculations

A tetrahedron method with Blöchl corrections was employed for the accurate electronic structure calculations, while other parameters remain the same as for the geometric relaxation. The average *p* / *d* state energy is calculated as the first moment of the density of states (DOSs) projected onto the atomic 2*p*-states / 5*d*-states of O / Ir atom relative to the Fermi level.

1.3. Reaction free energy calculations

The adsorption free energies of O*, OH* and OOH* were computed with reference to H_2 and H_2O in the gas phase. The vibrational frequencies of free molecules and adsorbates were

calculated by using the phonon modules in the VASP 5.3 code. A standard thermodynamic correction was applied to determine the free energy corrections, including the correction of the effect from zero-point energy, pressure, inner energy, and entropy. To accommodate for the influence from applied potential U, computational hydrogen electrode (CHE)[6] was adopted, where at a given $U \neq 0$ V vs. reversible hydrogen electrode (RHE), the chemical potential (μ) of proton and electron can be obtained through

$$\mu(H^+) + \mu(e^-) = \frac{1}{2}\mu(H_2) - eU$$

Therefore, the free energy change of e.g. OH* ↔ O* + ($H^+ + e^-$) can be calculated through

$$\Delta G = \mu(O^*) + \left[\frac{1}{2}\mu(H_2) - eU\right] - \mu(OH^*)$$

1.4. Distortion parameters

Four parameters, d_{mean}, ζ, Σ, and Θ have been adopted to quantify the degree of octahedron distortion. d_{mean} is defined as the average metal–ligand distances in the octahedral coordination sphere. ζ is defined as the average of the sum of the deviation of 6 unique metal–ligand bond lengths around the central metal atom from the average value. Σ is defined as the sum of the deviation of 12 unique *cis* ligand–metal–ligand angles from 90°. Θ is defined as the sum of the deviation of 24 unique torsional angles between the ligand atoms on opposite triangular faces of the octahedron viewed along the pseudo-threefold axis from 60°. All above parameters were computed using the OcatDist package.[7] We note that depending on their location, the degrees of distortion can be different for different [IrO_6] octahedrons on the same IrO_2 edge. Here all the distinct [IrO_6] octahedrons were considered as possible active sites, and their distortion parameters as well as reaction energetics were explicitly computed accordingly (see Tables S3 and S4 for more details).

2. Surface structure and termination

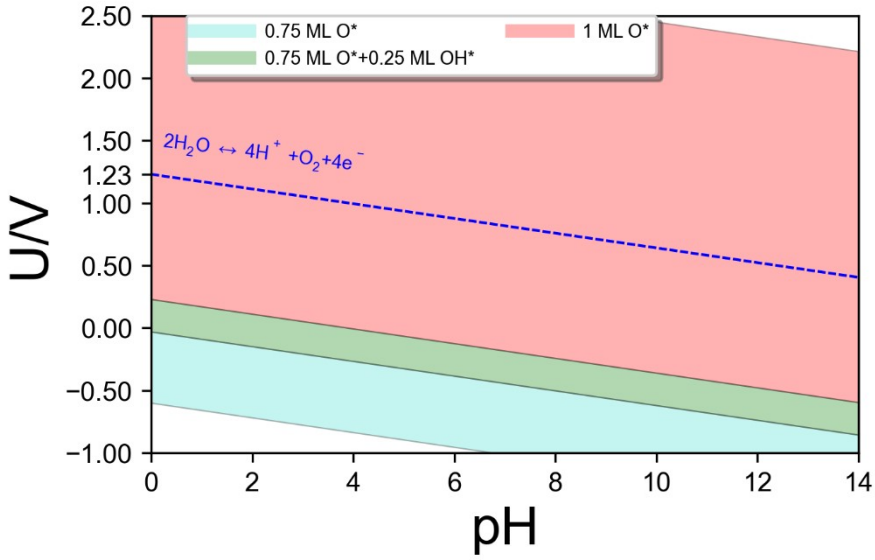

Fig. S1. The calculated surface Pourbaix diagram for the 3R-IrO_2 (003) facet.

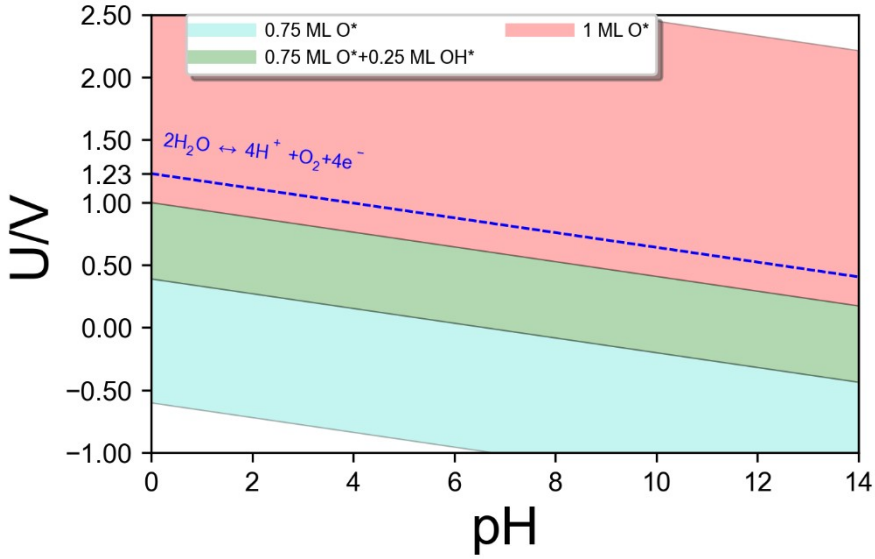

Fig. S2. The calculated surface Pourbaix diagram for the 3R-IrO_2 (012) facet.

The surface stability under acidic condition can be elucidated from the above Pourbaix diagrams. According to Figs. S1 and S2, the oxygen-covered surface remained stable across all pHs in the potential window relevant for OER. Given the structural similarity and oxygen

reactivity of various layered IrO_2 polymorphs, the identification of full O* coverage is applicable to all studied layered IrO_2 systems of interests.

3. Crystal structures of various layered IrO_2 polymorphs

For each polymorph, the edge surfaces with the second strongest calculated diffraction peaks were picked; while the strongest peaks are generally assigned to surfaces exposing the basal plane. In other words, the following crystal planes were considered for the edge sites: (011) (1T, 2H, 2Hr); (012) (1Tr, 3R, 3Rr).

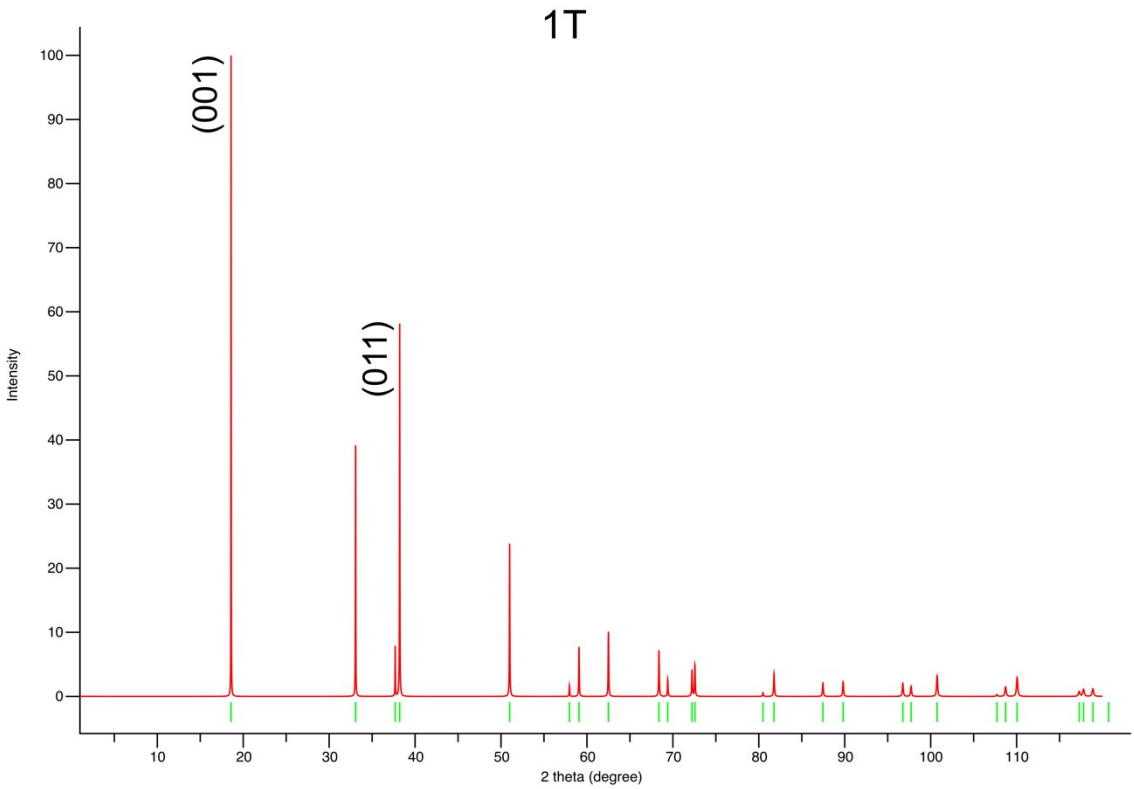

Fig. S3. The calculated X-ray diffraction pattern of IrO_2 bulk complying 1T structure.

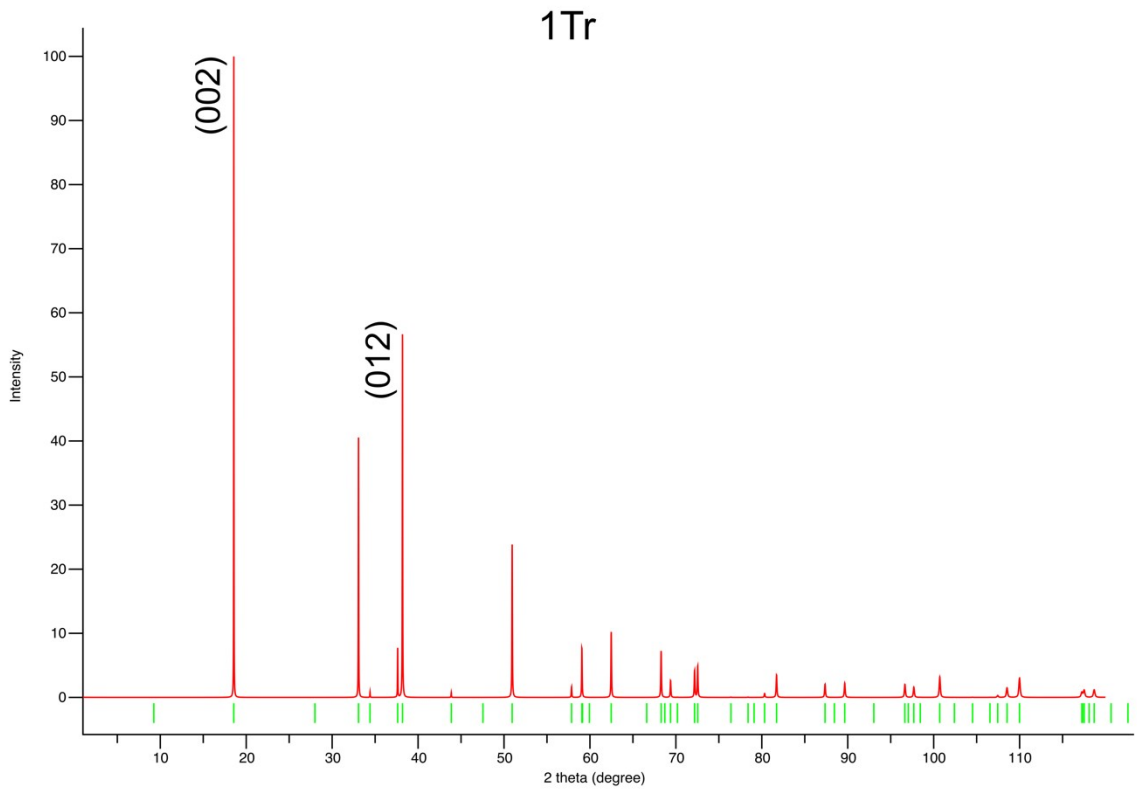

Fig. S4. The calculated X-ray diffraction pattern of IrO_2 bulk complying 1Tr structure.

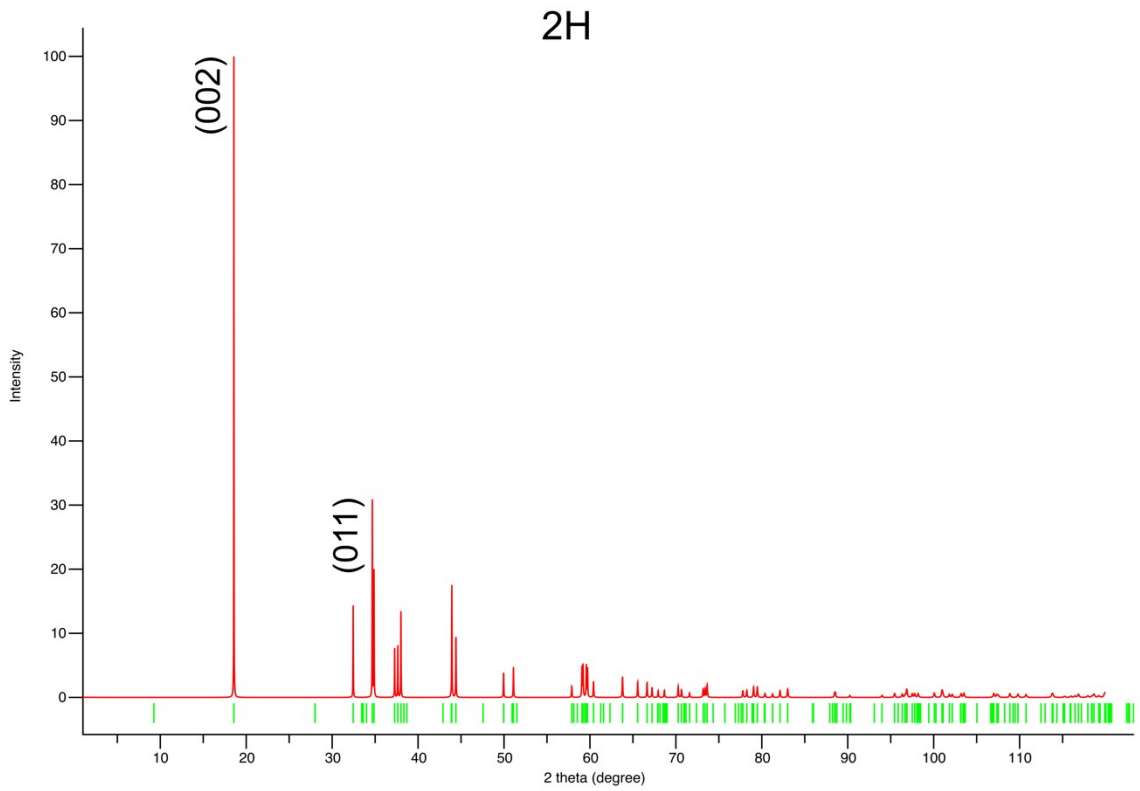

Fig. S5. The calculated X-ray diffraction pattern of IrO_2 bulk complying 2H structure.

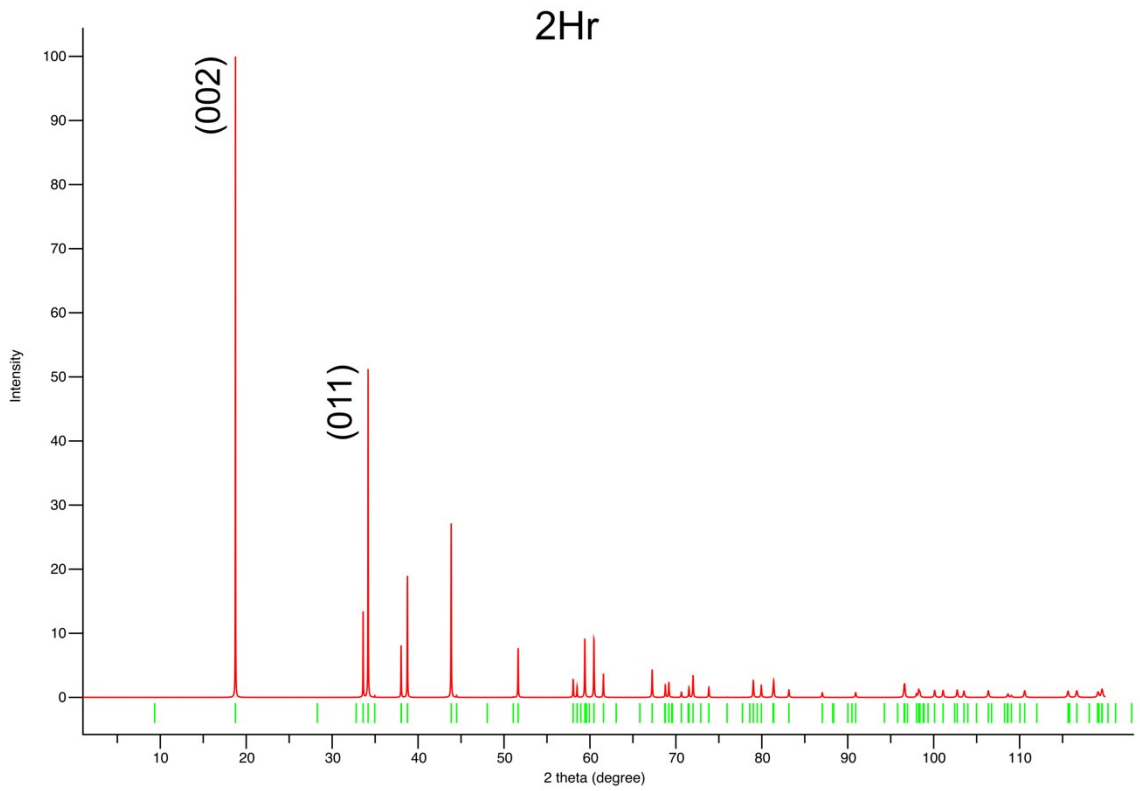

Fig. S6. The calculated X-ray diffraction pattern of IrO_2 bulk complying 2Hr structure.

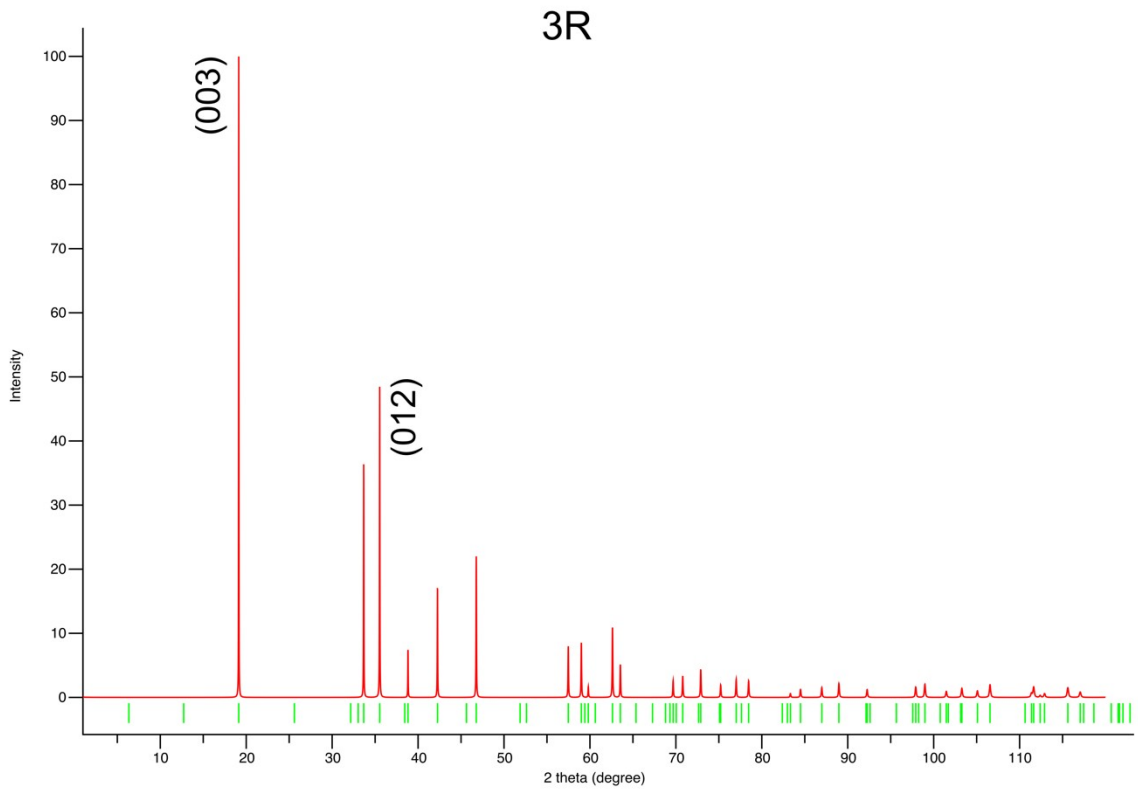

Fig. S7. The calculated X-ray diffraction pattern of IrO_2 bulk complying 3R structure.

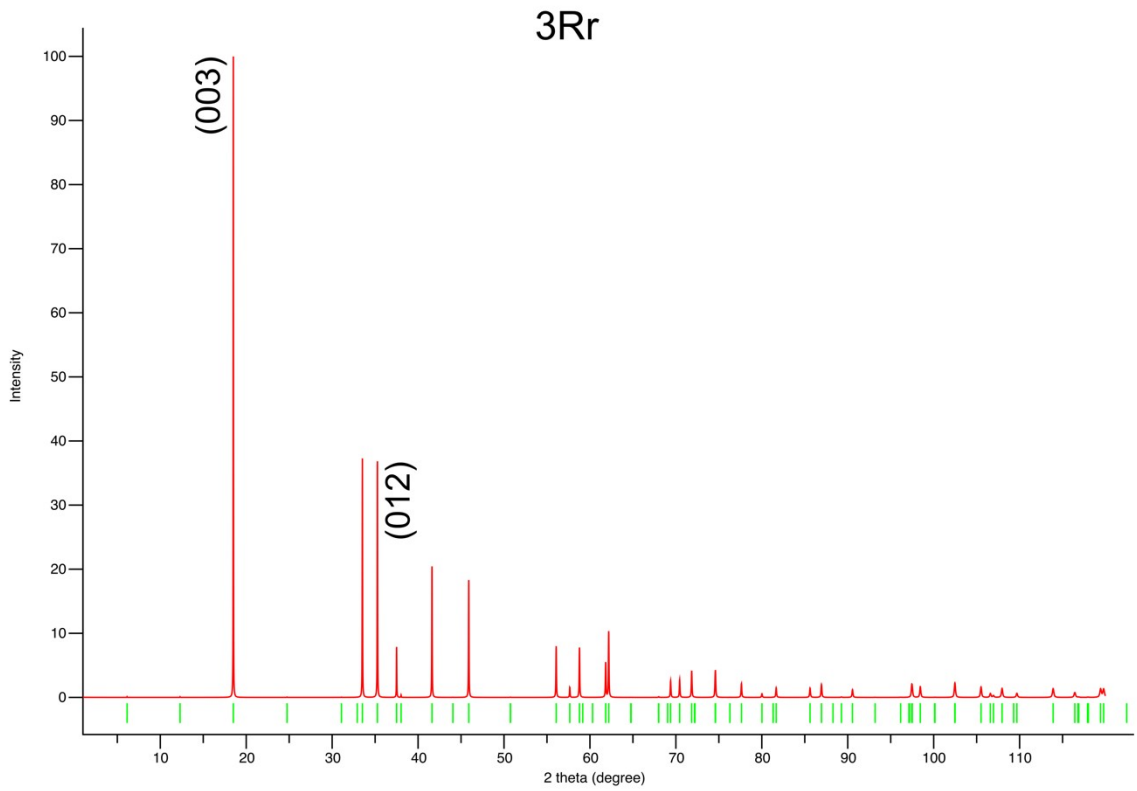

Fig. S8. The calculated X-ray diffraction pattern of IrO_2 bulk complying 3Rr structure.

4. Electronic structure analysis

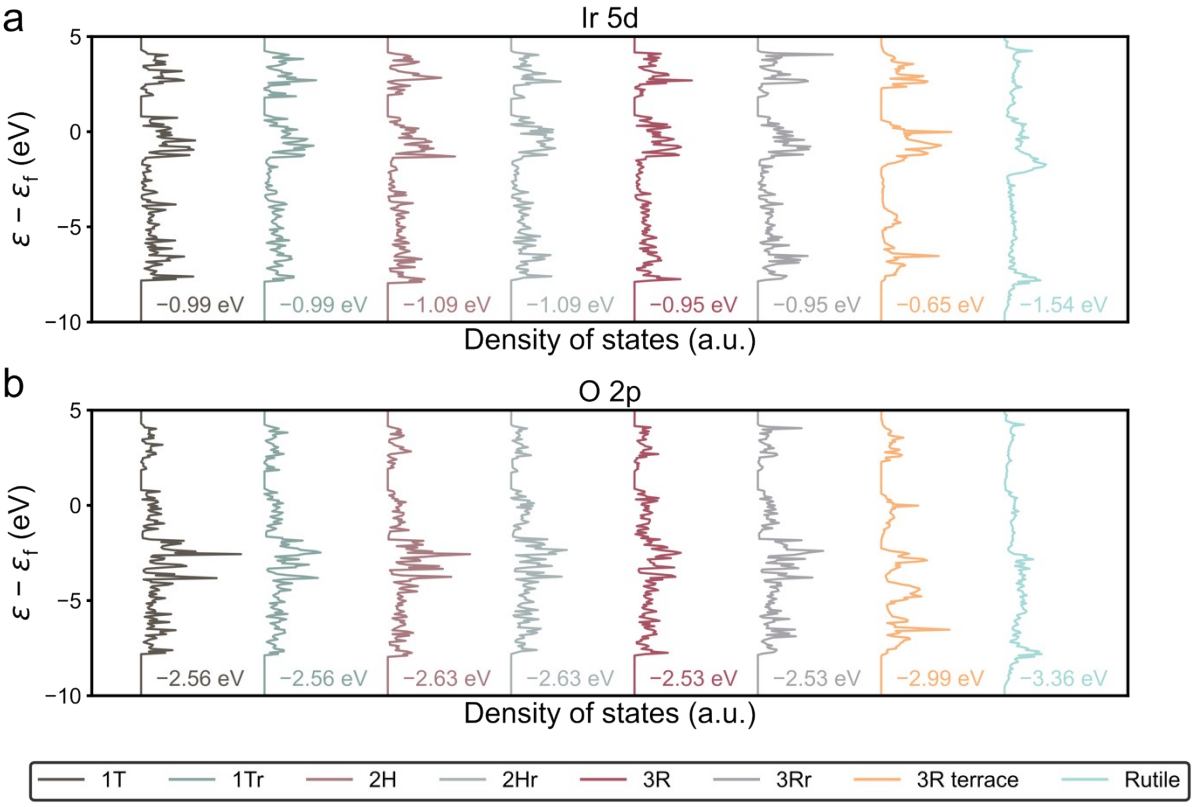

Fig. S9. The density of states projected onto (a) Ir-5*d* and (b) O-2*p* orbitals for different IrO_2. The corresponding $\bar{\varepsilon}_{Ir\_5d}$ and $\bar{\varepsilon}_{O\_2p}$ are annotated in the figure..

5. Demonstration of defected 3R-IrO_2

The structural stability of defected 3R-IrO_2 (with Ir vacancies at the edge, as shown in Fig. S10) can be quantified considering the reaction: $0.5O_2 + Ir_xO_y \rightarrow Ir_{x-1}O_{y-1} + IrO_2$. The corresponding formation energy of Ir vacancy can therefore be calculated through the following equation:

$$\Delta E_{Ir\_vacancy\_formation} = E_{Irx-1Oy-1} + E_{IrO2} - E_{IrxOy} + 0.5E_{O2}$$

where $E_{Irx-1Oy-1}$, E_{IrxOy} represents the electronic energies of defected IrO_2 and non-defected IrO_2, respectively, E_{IrO2} the energy of bulk 3R-IrO_2, E_{O2} the energy of oxygen gas. The Ir vacancy formation energy is 0.19 eV, at least 0.1 eV below the formation energy of layered IrO_2. Therefore, the creation of surface Ir vacancy on 3R-IrO_2 is thermodynamically possible under typical synthesis conditions.

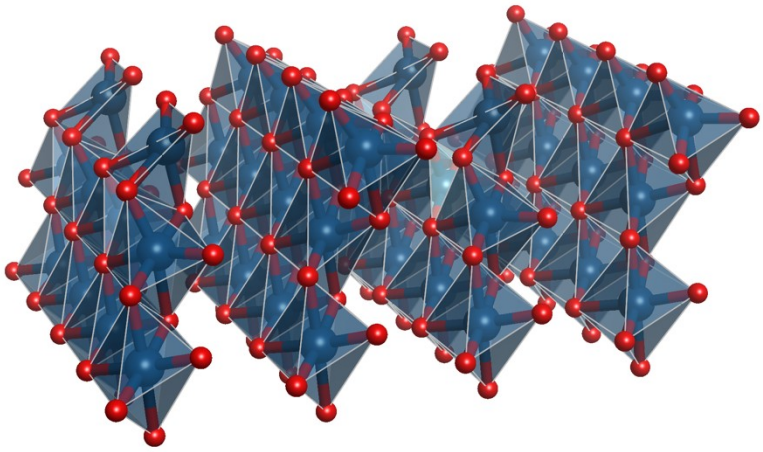

Fig. S10. Structure illustration of the defected surface based on 3R-IrO_2.

For defected 3R-IrO_2, both the lattice oxygen-mediated mechanism (LOM) and the adsorbate evolution mechanism (AEM) have been considered as a previous theoretical study by Alexandrov et al. has suggested that metal vacancies in rutile IrO_2 and RuO_2 favored LOM.[8] While AEM generally proceeds through the following steps:

$$H_2O_{(l)} + * \leftrightarrow OH* + (H^+ + e^-) \quad (1)$$

$$OH* \leftrightarrow O* + (H^+ + e^-) \quad (2)$$

$$H_2O_{(l)} + O* \leftrightarrow OOH* + (H^+ + e^-) \quad (3)$$

$$OOH* \leftrightarrow O_{2(g)} + * + (H^+ + e^-) \quad (4)$$

where the asterisk (*) indicates a certain surface specie or an empty site, LOM has a different pathway:

$$H_2O_{(l)} + * \leftrightarrow OH* + (H^+ + e^-) \quad (1)$$

$$OH* \leftrightarrow O* + (H^+ + e^-) \quad (2)$$

$$O* + O_{lattice} \leftrightarrow O_{2(g)} + \square + * \quad (5)$$

$$\square + H_2O_{(l)} \leftrightarrow OH_{lattice} + (H^+ + e^-) \quad (6)$$

$$OH_{lattice} \leftrightarrow O_{lattice} + (H^+ + e^-) \quad (7)$$

where □, $O_{lattice}$, and $OH_{lattice}$ refer to oxygen vacancy, lattice oxygen, and hydroxyl filled in the oxygen vacancy, respectively. The step (5) is constantly the reaction step requiring the highest Gibbs free energy change at OER-relevant potentials (≥ 1.23 V vs. RHE) in LOM on defected 3R-IrO_2. It can be seen from Fig. S11 that while LOM was preferred at lower potential (e.g. 1.23 V vs. RHE), AEM soon starts to dominate at typical OER working potential (e.g. ≥ 1.5 V). In addition, experimental evidence has revealed that AEM remained the major pathway on layered IrO_2.[9] Therefore, AEM was chosen as the relevant pathway to demonstrate the catalytic potential of defected 3R-IrO_2.

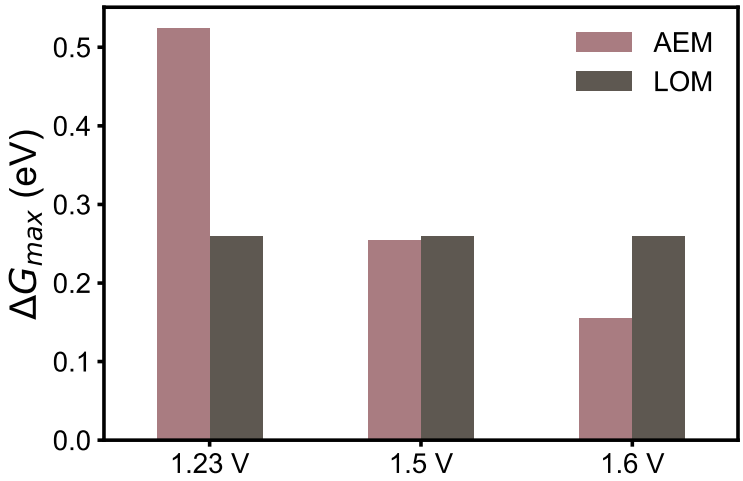

Fig. S11. Comparison of the maximum reaction energies (ΔG_{max}) for AEM and LOM pathways under different potentials.

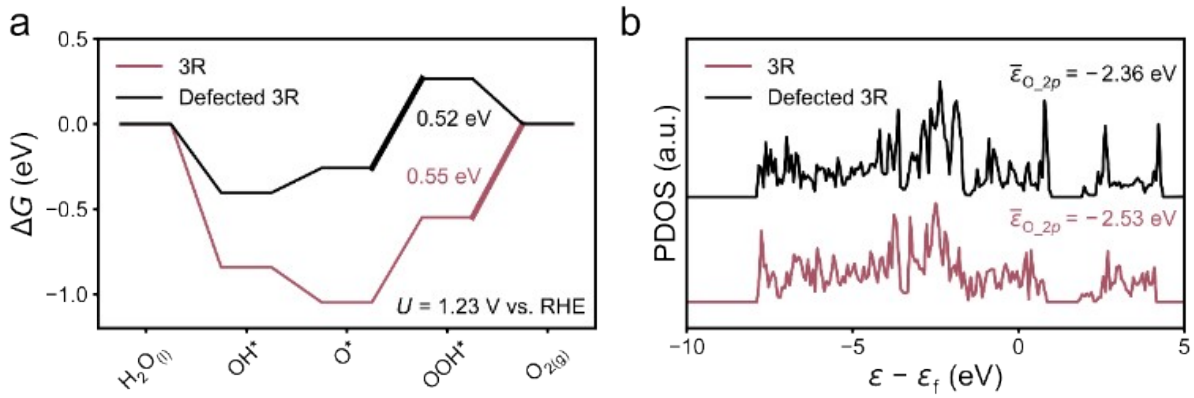

Fig. S12. (a) Free energy diagrams of OER on 3R-IrO_2 edge (puce) and defected 3R-IrO_2 edge (black) at U = 1.23 V vs. RHE. Bold lines indicate the PLSs. (b) PDOS of O-2*p* orbitals of O*-adsorbed 3R-IrO_2 and defected 3R-IrO_2.

6. Supplementary Tables

Table S1. The formation energy of different layered IrO_2 above the hull (ΔE_{hull}) relative to the most stable rutile-IrO_2 tetragonal phase.

Name	ΔE_{hull} (eV)
1T	0.310
1Tr	0.307
2H	0.306
2Hr	0.308
3R	0.310
3Rr	0.307

While all layered IrO_2 exhibit similar stabilities and are metastable phases with roughly 0.3 eV atom^{-1} uphill in terms of formation energy above the hull (ΔE_{hull}) relative to the most stable rutile-IrO_2 tetragonal phase, this value is well below the amorphous limit for IrO_2 (ΔE_{hull} of approximately 0.5 eV[10]), aligning with experimentally validated synthesizability.[11, 12] Moreover, the most stable surface of layered IrO_2 (e.g. the (003) surface of 3R-IrO_2) exhibits a promisingly low surface energy (−0.07 eV Å^{-2}) when compared to that of the most stable (110) surface of rutile-IrO_2 (0.26 eV Å^{-2}), further demonstrating the relative stability of layered IrO_2 phases in the form of thin sheets.

Table S2. The calculated overpotential (η) and the potential-limiting step (PLS) for the terrace sites on different IrO_2.

Name	η (V)	PLS	Name	η (V)	PLS
1T (001)	1.82	O* -> OOH*	2Hr (002)	1.93	O* -> OOH*
1Tr (002)	1.82	O* -> OOH*	3R (003)	1.83	O* -> OOH*
2H (002)	1.79	O* -> OOH*	3Rr (003)	1.82	O* -> OOH*

Table S3. The calculated η and PLS for the edge sites on different IrO_2.

Name	η (V)	PLS
1T	0.71	O* -> OOH*
1Tr (site 1)	0.62	O* -> OOH*
1Tr (site 2)	0.71	O* -> OOH*
2H	0.72	O* -> OOH*
2Hr (site 1)	0.66	OOH* -> O_2
3R	0.55	OOH* -> O_2
3Rr (site 1)	0.72	O* -> OOH*
3Rr (site 2)	0.56	O* -> OOH*
3Rr (site 3)	0.63	O* -> OOH*

Table S4. The calculated geometric and electronic-structure parameters for the off-scaling energetic analysis.

Name	q_{bader}	$\bar{\epsilon}_{O\_2p}$	$\bar{\epsilon}_{Ir\_5d}$	ζ	Mag	d_{mean} (Å)	Σ	Θ
1T	0.45	−2.56	−0.99	0.54	0.30	1.98	115.34	286.62
1Tr (site 1)	0.47	−2.52	−0.91	0.53	0.29	1.98	114.96	277.51
1Tr (site 2)	0.45	−2.52	−0.91	0.54	0.29	1.98	117.49	289.15
2H	0.46	−2.63	−1.09	0.56	0.30	1.98	111.82	265.49
2Hr (site 1)	0.45	−2.52	−0.91	0.52	0.29	1.99	120.71	305.61
3R	0.46	−2.53	−0.95	0.55	0.28	1.98	118.60	299.51
3Rr (site 1)	0.45	−2.71	−1.10	0.54	0.30	1.98	117.33	286.14
3Rr (site 2)	0.47	−2.71	−1.10	0.54	0.28	1.98	116.34	289.59
3Rr (site 3)	0.46	−2.71	−1.10	0.54	0.28	1.98	117.47	292.21

Table S5. The hydrogen bond analysis for the interaction between OOH* and the nearby lattice O atom (O–H…$O_{lattice}$) on various IrO_2 surfaces. The bond length is identified as the distance between O and $O_{lattice}$.

Name	Bond length (Å)	Angle (°)	Name	Bond length (Å)	Angle (°)
1T	3.67	101	3R	2.82	104
1Tr (site 1)	3.56	137	3Rr (site 1)	3.82	101
1Tr (site 2)	3.67	104	3Rr (site 2)	2.86	147
2H	3.52	101	3Rr (site 3)	2.69	135
2Hr (site 1)	3.60	72	Rutile	4.04	90

According to the above analysis, the OOH* adsorption on the site 1 of 2Hr-IrO_2 shows an O–H…$O_{lattice}$ angle well below the lower limit of 90°; whereas the OOH* adsorption on rutile-IrO_2 shows that the O–H…$O_{lattice}$ bond length exceeds the upper limit of 4.00 Å and the angle is exactly 90°. Therefore, the above two surfaces exhibit negligible hydrogen bonding with OOH*; while other surfaces show hydrogen bonding with bond lengths and angles in the typical range of moderate hydrogen bonds. Nevertheless, either O–H…$O_{lattice}$ bond length or angle alone poorly correlates to the degree of OOH* stabilization ($\Delta\Delta G_{OOH*}$), indicating that the hydrogen bonding effect cannot solely account for the scaling breaking on layered IrO_2 edges.

7. Supplementary References

1. G. Kresse and J. Furthmuller, *Comp. Mater. Sci.*, 1996, **6**, 15-50.
2. G. Kresse and J. Furthmuller, *Phys. Rev. B*, 1996, **54**, 11169-11186.
3. J. P. Perdew, K. Burke and M. Ernzerhof, *Phys. Rev. Lett.*, 1996, **77**, 3865-3868.
4. G. Kresse and D. Joubert, *Phys. Rev. B*, 1999, **59**, 1758-1775.
5. H. J. Monkhorst and J. D. Pack, *Phys. Rev. B*, 1976, **13**, 5188-5192.
6. J. K. Norskov, J. Rossmeisl, A. Logadottir, L. Lindqvist, J. R. Kitchin, T. Bligaard and H. Jonsson, *J. Phys. Chem. B*, 2004, **108**, 17886-17892.
7. R. Ketkaew, Y. Tantirungrotechai, P. Harding, G. Chastanet, P. Guionneau, M. Marchivie and D. J. Harding, *Dalton Trans.*, 2021, **50**, 1086-1096.
8. A. Zagalskaya and V. Alexandrov, *ACS Catal.*, 2020, **10**, 3650-3657.
9. J. L. Tang, X. Y. Liu, X. X. Xiong, Q. S. Zeng, Y. Ji, C. X. Liu, J. W. Li, H. L. Zeng, Y. Z. Dai, X. Y. Zhang, C. B. Li, H. J. Peng, Q. Jiang, T. T. Zheng, C. W. Pao and C. Xia, *Adv. Mater.*, 2024, **36**, 2407394.
10. R. A. Flores, C. Paolucci, K. T. Winther, A. Jain, J. A. G. Torres, M. Aykol, J. Montoya, J. K. Norskov, M. Bajdich and T. Bligaard, *Chem. Mater.*, 2020, **32**, 5854-5863.
11. Q. Dang, H. P. Lin, Z. L. Fan, L. Ma, Q. Shao, Y. J. Ji, F. F. Zheng, S. Z. Geng, S. Z. Yang, N. N. Kong, W. X. Zhu, Y. Y. Li, F. Liao, X. Q. Huang and M. W. Shao, *Nat. Commun.*, 2021, **12**, 6007.
12. Z. L. Fan, Y. J. Ji, Q. Shao, S. Z. Geng, W. X. Zhu, Y. Liu, F. Liao, Z. W. Hu, Y. C. Chang, C. W. Pao, Y. Y. Li, Z. H. Kang and M. W. Shao, *Joule*, 2021, **5**, 3221-3234.